



Self-dressing Rydberg atomic receiver based on laser-induced DC field



Jinhao Zhang^{1,2,3}, Zhanshan Sun^{1,3}, Jiawei Yao², Fengting Zhao¹, Yi Lin¹, Di Sang¹, Kai Yang¹, Qiang An¹ ✉ & Yunqi Fu¹ ✉

Rydberg atomic receiver holds distinctive advantages of ultra-wide operating bandwidth and inherently high sensitivity in electric field measurement¹, in particular, it promises unique superiority of miniaturization for low-frequency especially kHz-band signals, which hold pivotal value in applications such as long-range navigation, ground-penetrating radar, and underwater communication. However, the capability of kHz atomic receivers remains severely constrained by the shielding effects of adsorbed alkali metal atoms. Here, we propose a conceptually new self-dressing kHz signal measurement paradigm by converting the undesired coupling-laser-induced DC field to an atomic dressing, and deftly building atomic superheterodyne inside the sapphire vapor cell, which is prepared to adequately suppress the low-frequency shielding through resistivity manipulation engineering. Further, we realize strengthened interaction between the atoms and kHz field by localized enhancement of the incident signals, and finally achieve an ultrahigh sensitivity of $13.5 \text{ nV/cm/Hz}^{1/2}$ at 100 kHz. This architecture represents a significant advance, with the potential to greatly accelerate the practical applications of Rydberg atomic receivers in kHz-band detection, communication, and related fields.

Quantum sensing technology has made transformative progress in the last decade, particularly in the fields of quantum magnetometers^{2–5}, electrometers^{6–8}, and gravimeters^{9–11}. Rydberg atom-based sensors demonstrate impressive electric field measurement capabilities, including ultra-broadband operating range (kHz–THz), wavelength-independent detection, and traceability to SI standards^{12–21}. One central research focus is to improve the measurement sensitivity, and this has been highlighted by recent experiments that the sensitivity was enhanced to several $\text{nV/cm/Hz}^{1/2}$ for microwave fields^{22–24}. Besides, unlike conventional antennas constrained by the Chu limit, Rydberg atoms enable electromagnetic signal reception using compact vapor cells (centimeter-scale). Consequently, it promises unique superiority of miniaturization for low-frequency, especially kHz-band, and shortwave signals^{25–30}. This renders Rydberg atomic sensors inherently size-friendly for the practical applications in low-frequency domains, including remote navigation, underwater communication, and ground-penetrating detection.

However, for low-frequency signal measurement, the shielding effects driven from the adsorption of alkali metal atoms inside vapor cells cause severe attenuation for the electric fields, seriously suppressing the detection sensitivity of Rydberg atoms. There are two rational approaches to weaken or to avoid the shielding impacts: (1) Adopting vapor cells with built-in

electrodes to directly inject the signals into the cell through metal plates and operate the electric field measurement. Though a highly sensitive response of Rydberg atoms to quasi-DC and kHz signals has been verified^{31,32}, the injection methods may require a supplementary receiving aperture to collect the spatial electric field and feed signals via a current-conducted way. (2) Preparing high-resistivity sapphire vapor cells to suppress the adsorption of alkali metal atoms^{33,34}. This has notably improved the atomic sensing capability, but the current optimal sensitivity is limited to a few $\mu\text{V/cm/Hz}^{1/2}$, indicating that developing new sensing techniques to further enhance sensitivity is still a tricky challenge.

While DC field dressing strategies have recently shown potential for enhancing sensitivity in kHz bands, metastable interface effects—particularly alkali metal adsorbate-mediated negative electron affinity (NEA), exclusively disrupt the generation of DC electric field via external drives such as the illumination of long-wavelength lasers^{35–37}. High-energy LED can successfully excite a stronger photoelectric effect to form a strengthened DC field, but it may counterproductively exacerbate the shielding effects of the vapor cells. Here, we demonstrate a conceptually new self-dressing kHz signal atomic receiver based on a laser-induced DC field, achieving direct reception of spatial kHz signals with a remarkably high sensitivity of $0.75 \mu\text{V/cm/Hz}^{1/2}$ at 100 kHz. This architecture leverages sapphire to modulate the adsorption

¹College of Electronic Science and Technology, National University of Defense Technology, Changsha, Hunan, China. ²Northwest Institute of Nuclear Technology, Xi'an, Shaanxi, China. ³These authors contributed equally: Jinhao Zhang, Zhanshan Sun. ✉e-mail: anqiang18@nudt.edu.cn; yunqifu@nudt.edu.cn

dynamics of alkali metal atoms, thereby suppressing NEA within vapor cells. Additionally, a spatial field resonant enhancement structure (RES) is introduced to coordinate with the low-shielding vapor cells, extremely strengthening the interaction between atoms and the kHz field and achieving an ultrahigh sensitivity of 13.5 nV/cm/Hz^{1/2}. This architecture is expected to significantly advance the applications of Rydberg atomic receivers in detection and communication in the kHz-band.

Results

Theory of kHz signal measurement using Rydberg atoms

We consider a three-level Rydberg atom model (Fig. 1b) (Methods). When measuring kHz signals using the AC Stark effect, the Rydberg state |52D_{5/2}) undergoes a shift under the influence of the signal field, and its Rabi frequency shows a corresponding relationship with the intensity of the signal field:

$$\Omega_{\text{stark}} = -\alpha E_{\text{tot}}^2/2 \quad (1)$$

Herein, α represents the polarizability of atomic energy levels with respect to the signal electric field, and E_{tot} denotes the total electric field applied to the atoms.

In the scenario of receiving time-harmonic signals, where $E_{\text{tot}} = A_{\text{sig}} \cos(\omega_{\text{sig}}t + \phi_{\text{sig}})$, we can get the Rabi frequency $\Omega_{\text{stark}} = -\alpha A_{\text{sig}}^2 [\cos(2\omega_{\text{sig}}t + 2\phi_{\text{sig}}) + 1]/4$. The distance of the energy level shift exhibits a quadratic relationship with the amplitude of the electric field. When an auxiliary DC field is introduced, E_{tot}^2 transforms into:

$$\begin{aligned} E_{\text{tot}}^2 &= (E_{\text{DC}} + E_{\text{sig}} \cos(\omega_{\text{sig}}t + \phi_{\text{sig}}))^2 \\ &= E_{\text{DC}}^2 + E_{\text{sig}}^2/2 + E_{\text{sig}}^2 \cos(2\omega_{\text{sig}}t + 2\phi_{\text{sig}})/2 \\ &\quad + 2E_{\text{DC}}E_{\text{sig}} \cos(\omega_{\text{sig}}t + \phi_{\text{sig}}) \end{aligned} \quad (2)$$

When $E_{\text{DC}} \gg E_{\text{sig}}$, the formula can be simplified to:

$$E_{\text{tot}}^2 \approx E_{\text{DC}}^2 + 2E_{\text{DC}}E_{\text{sig}} \cos(\omega_{\text{sig}}t + \phi_{\text{sig}}) \quad (3)$$

The corresponding Rabi frequency of the Stark shift is:

$$\begin{aligned} \Omega_{\text{stark}} &= -\alpha E_{\text{DC}}^2/2 - \alpha E_{\text{DC}}E_{\text{sig}} \cos(\omega_{\text{sig}}t + \phi_{\text{sig}}) \\ &= \Omega_0 - \alpha E_{\text{DC}}E_{\text{sig}} \cos(\omega_{\text{sig}}t + \phi_{\text{sig}}) \end{aligned} \quad (4)$$

When measuring kHz signals, the auxiliary DC field can act as an enhancement factor to boost the Rabi frequency of energy level shifts and convert the second-order response into a first-order linear response. After locking the coupling laser frequency at a designated position on the spectrum, the Stark shift generated by atomic energy levels can be converted into a change in optical power, thereby producing a voltage signal with the corresponding kHz frequency at the output of the photodetector, where $\tilde{V}_{\text{sig}} = \beta \cdot \tilde{\Omega}$. Here, β represents the slope of the electromagnetically induced transparency (EIT) spectrum at the locked frequency point of the coupling laser, and $\tilde{\Omega} = -\alpha E_{\text{DC}}E_{\text{sig}} \cos(\omega_{\text{sig}}t + \phi_{\text{sig}})$ denotes the AC term in the variation of the Rabi frequency of the Stark shift.

Analysis of the induced DC field

Owing to the low-frequency shielding effect of the alkali metal vapor cell walls, electric fields with lower frequencies are more difficult to penetrate into the cell, so that external DC fields nearly cannot be applied to Rydberg atoms. Currently, there are two main methods to apply a DC field inside the cell. One is to construct built-in electrodes that penetrate through the cell walls. This method can directly inject low-frequency signals into the vapor cell, thereby verifying the response capability of Rydberg atoms to low-frequency signals. However, when directly receiving spatial electric fields, this method is still limited by the short-circuit effect of cell walls, severely degrading the reception performance. The other method is to irradiate the cell wall with short-wavelength LED light in a modest way. The given light induces the photoelectric effect and generates charges accumulated at the light spot, thereby creating a built-in DC field inside the cell without modifying the cell structure.

For cesium metal, the typical value of its work function Φ_{Cs} is 1.95 eV, corresponding to the longest wavelength $\lambda_0 = hc/\Phi_{\text{Cs}} \approx 636\text{nm}$ for inducing the photoelectric effect, where h is the Planck constant and c is the speed of light in vacuum. When constructing a three-level system, the

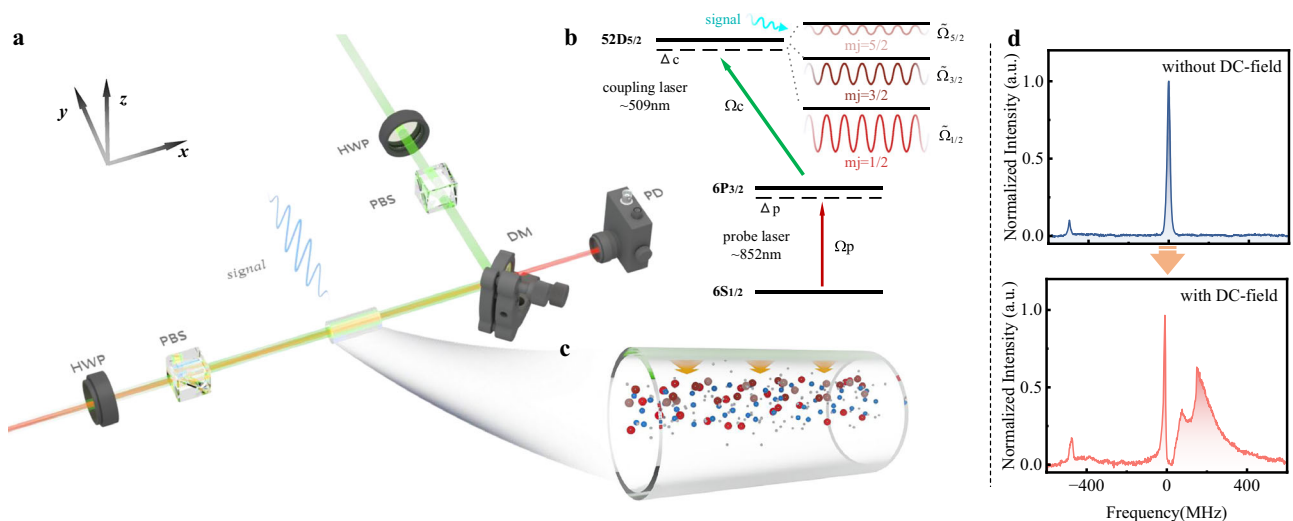


Fig. 1 | Schematic diagram of the Rydberg atom receiver based on self-dressing of laser-induced DC field. **a** Overview of the experimental setup. The following symbols are used: (1) PBS: Polarizing Beam Splitter, (2) HWP: Half-Wave Plate, (3) DM: Dichroic Mirror, (4) PD: Photodetector. **b** Level scheme. The probe laser excites cesium atoms from the ground state |6S_{1/2}) to the excited state |6P_{3/2}); the coupling laser excites atoms from the excited state |6P_{3/2}) to the Rydberg state |52D_{5/2}). Δp and Δc are the detunings of the probe laser and coupling laser from the resonant frequencies between energy levels, respectively. Under the self-dressing effect of the laser-induced DC field, the magnetic sublevels of the Rydberg state |52D_{5/2}) undergo

degeneracy lifting, and the energy levels exhibit a time-dependent position $\tilde{\Omega}$ under the action of the signal field. **c** Schematic of the laser-induced DC field inside the vapor cell. When the coupling laser is incident near the cell wall, the DC field generated by positive charge clusters excited on the cell wall via the photoelectric effect acts on Rydberg atoms. The yellow arrows in the figure indicate the vector direction of the DC field. **d** Spectral diagram of the degeneracy lifting of the Rydberg state |52D_{5/2}) under the self-dressing effect, by monitoring the probe laser transmitted through the vapor cell while scanning the coupling laser frequency (Methods).

wavelength of the coupling laser used to excite cesium atoms to the Rydberg state is 509 nm. This laser theoretically satisfies the conditions for inducing a DC field inside the cell. However, since commonly used glass cell walls have a significant NEA, the process of negative charge adsorption greatly weakens the strength of the electrostatic field³⁷, rendering this electric field merely a perturbation term that broadens the EIT spectrum.

In this work, sapphire material is employed to modify such adsorption dynamics, mitigating the adsorption of negative charges during the photoelectric effect. This enables the generation of built-in potential induced by the coupling laser with sufficient strength to modulate the atomic energy levels, thereby transforming the stray electric field—previously regarded as a “detrimental factor”—into an energy level-dressing electric field to enhance the reception of kHz signals (Fig. 1c). Due to the enclosed nature of the vapor cell, the DC electric field induced by the coupling laser inside the cell is difficult to measure via traditional methods. Therefore, the field intensity is obtained by analyzing the DC Stark energy level shift of the probe laser (Fig. 1d). As shown in Fig. 2, when the beam is positioned 2.4 mm below the top wall of the cell, the relationship between the DC electric field strength and the coupling laser power is measured. By varying the coupling laser power, the three sublevels ($m_j = 1/2, 3/2, 5/2$) of the $52D_{5/2}$ state exhibit significant Stark shifts proportional to their respective polarizabilities, leading to the lifting of degeneracy. Calculations using the Alkali Rydberg Calculator (ARC) show that the polarizabilities α_j of these sublevels are $-1867 \text{ MHz cm}^2 \text{ V}^{-2}$, $-1227 \text{ MHz cm}^2 \text{ V}^{-2}$, and $101 \text{ MHz cm}^2 \text{ V}^{-2}$, respectively. Therefore, the $m_j = 1/2$ sublevel has the largest polarizability and thus shows the most significant Stark frequency shift under the same electric field, making it highly suitable for kHz signal measurement (Methods). By scanning the coupling laser frequency, the spectral distance between the Rydberg state fine levels $52D_{3/2}$ and $52D_{5/2}$ can be used to calibrate the abscissa of the EIT spectrum, thereby achieving an accurate frequency reference.

Analysis of low-frequency shielding

Alkali metal vapor is typically enclosed within dielectric containers, such as glass vapor cells fabricated from borosilicate materials. As signals traverse the cell walls, they undergo inevitable disturbance in both amplitude and phase. Notably, the deposition of alkali metal atoms on the inner surfaces of the vapor cell forms a conductive layer with low sheet resistance. Charges within this layer redistribute under the influence of external electric fields, partially canceling the field that penetrates into the vapor cell. This phenomenon severely impedes the transmission of kHz signals, giving rise to the so-called low-frequency shielding effect. For quantitative analysis of this effect, we model the cell as a spherical shell with negligible thickness. For an external unit step electric field signal, the resultant electric field inside the cell is given by $E_{in}(t) = \exp(-t/1.5\epsilon R_{\square} r)^{33}$. The conversion of time-frequency

domain via the Fourier transform yields the transfer function $T(f)$ which demonstrates the relationship between the internal and external electric fields of the cell (Methods):

$$T(f) = \frac{j2\pi f}{1/(1.5\epsilon R_{\square} r) + j2\pi f} \quad (5)$$

Due to the differences in the adsorption of alkali metal atoms for sapphire and glass materials, the sheet resistances of cells made from these two materials exhibit significant disparities, and thus, the amplitudes of electric fields penetrating through the cell walls vary considerably. As the frequency of the electric field decreases, the shielding effect becomes more pronounced. For the kHz band, the amplitude attenuation even increases by several orders of magnitude for normal vapor cells. With the increase of measurement frequency, the difference of transmitted amplitudes between sapphire and glass materials gets smaller (Fig. 3a). This proves that sapphire cells have stronger coupling capability to spatial electric fields in the kHz band. Extending this derivation to more general-shaped cells, the electric field can be calculated as $E_{in}(t) = \exp(-2\gamma t)$, where the coefficient 2 arises from the quadratic response relationship of the electric field³³. The shielding factor γ has the dimension of s^{-1} and reflects the response speed of charge redistribution on the cell walls, i.e., the faster the response speed, the more significant attenuation of the cell on signals of the same frequency. Thus, we can obtain a more general transfer function formula (Methods):

$$T(f) = \frac{j\pi f}{\gamma + j\pi f} = \frac{\pi f}{\sqrt{\gamma^2 + (\pi f)^2}} \cdot \exp(j\arctan(\gamma/\pi f)) \quad (6)$$

Using atomic low-frequency superheterodyne technology, we measured the response of the Rydberg atomic sensor to electric field signals under different coupling laser powers, while the probe laser power is fixed at $120 \mu\text{W}$ (Fig. 3b). Since the polarizability of Rydberg atoms varies minimally in the kHz band, this response curve directly reflects the changes in the amplitude of transfer function $T(f)$. Based on the characteristics of the amplitude curve of $T(f)$, we fitted the shielding factor γ using orthogonal distance regression.

When increasing the power of the coupling laser, the frequency of shielding effect occurrences gets higher, indicating a more pronounced low-frequency shielding phenomenon. Notably, even with lower coupling laser power, the introduction of LED light for inducing a DC electric field exacerbates the low-frequency shielding effect—this is likely due to LED light exciting more free electrons on the cell wall surface.

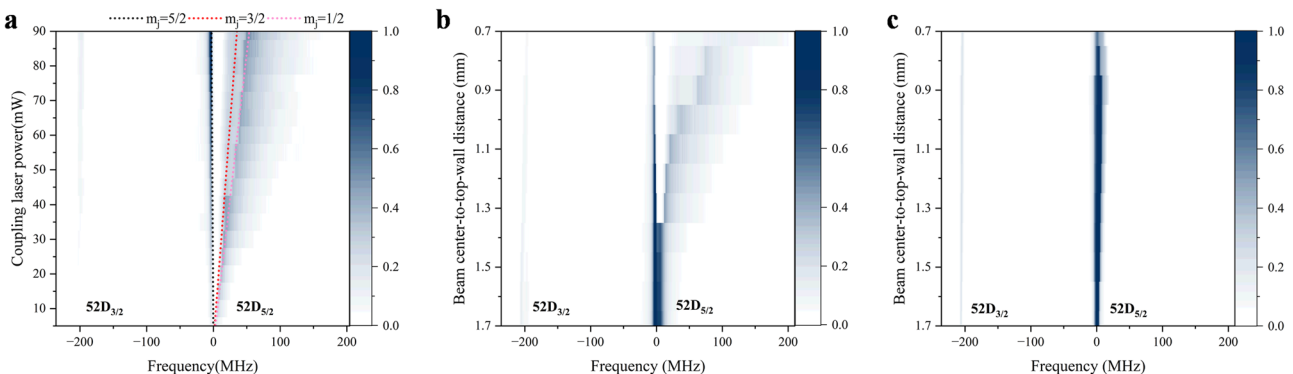


Fig. 2 | Spectra of atomic energy levels affected by the self-dressing effect of DC fields. **a** Variations in the Stark shift of the $|52D_{5/2}\rangle$ sublevel induced by changing the coupling laser power, with the laser beam fixed 2.4 mm below the upper wall of the sapphire vapor cell. **b** Variations in the Stark shift of the $|52D_{5/2}\rangle$ sublevel induced by changing the position of the laser beam relative to the cell wall, with the coupling

laser power fixed at 90 mW and the laser beam positioned directly below the upper wall of the sapphire vapor cell. **c** Variations in the Stark shift of the $52D_{5/2}$ sublevel induced by changing the position of the laser beam relative to the cell wall of the glass cell, with all other conditions identical to those in (b).

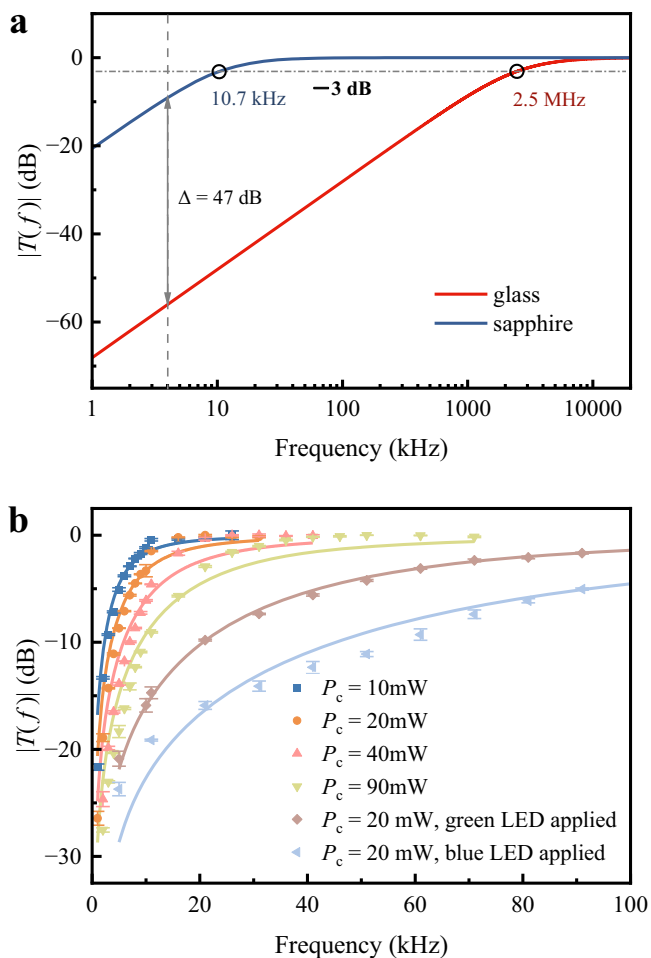


Fig. 3 | Relationship between the amplitude of transfer function T and frequency. **a** Variation curves of $|T(f)|$ measured using a conventional glass vapor cell and a sapphire vapor cell, respectively, with the probe laser power fixed at $120 \mu\text{W}$ and the coupling laser power at 20 mW . Black circles in the figure mark the positions where $|T(f)|$ decreases by 3 dB, and vertical gray lines mark the difference value when the curves tend to be parallel as frequency decreases. **b** Variation curves of $|T(f)|$ measured under different coupling laser powers (P_c) and external LED illumination conditions, with the laser beam fixed 2.4 mm below the cell wall. For external LED illumination, the illumination range covers the region from the top of the vapor cell to 1 mm below it to generate a vertically polarized DC field; the green LED power is 78 mW , and the blue LED power is 88 mW .

Thus, using the self-dressing effect based on DC fields excited by coupling laser for kHz signal reception can minimize the low-frequency shielding effect, achieving the dual benefits in simplifying the system architecture and optimizing the reception performance of the sensor.

Signal reception based on low-frequency atomic super-heterodyne technology

Based on the above analysis, the primary factors influencing the measurement sensitivity of kHz signals are the slope β of the EIT spectrum, the transfer function $T(f)$, the strength E_{DC} of the DC electric field, and the polarizability α_j . Here, we select the sublevel $m_j = 1/2$ for measurement and optimize the coupling laser power to determine the optimal parameter settings for the atomic sensor. When the signal intensity is lower than the noise intensity V_{noise} , the information contained in the signal is difficult to extract effectively. Therefore, we define the minimum detectable signal as $V_{\text{min}} = V_{\text{noise}}$, and the sensitivity can be expressed as:

$$S = E_{\text{min}} / \sqrt{RBW} = -V_{\text{min}} / (|T(f)| \alpha \beta E_{\text{DC}} \sqrt{RBW}) = \sqrt{P_{\text{min}} R} / d \sqrt{RBW} \quad (7)$$

Herein, the minimum detectable electric field strength is denoted as E_{min} . P_{min} represents the output power of the signal source when the output voltage of the PD is V_{min} . The resolution bandwidth (RBW) of the spectrum analyzer is set to 1 Hz when receiving the output signal of the PD. d is the distance between the core plate and the floor of the TEM cell for generating kHz spatial signal fields (Methods)³⁸.

In this work, the sensitivity of the atomic sensor was measured at 20 and 100 kHz to verify its application in important fields such as underwater communication and remote navigation. The probe laser power was set to $120 \mu\text{W}$, and the coupling laser power was set to 12.4 and 50.3 mW when measuring 20 and 100 kHz signals, respectively, with the beam positioned 2.4 mm below the upper wall of the cell. For a measurement duration of 1 s , the minimum detectable electric fields at 20 kHz and 100 kHz were 1.33 and $0.75 \mu\text{V}/\text{cm}$, corresponding to sensitivities of 1.33 and $0.75 \mu\text{V}/\text{cm}/\text{Hz}^{1/2}$, respectively. Compared with measurements using the second-order Stark effect without a DC field, the sensitivity was enhanced by a factor of 508 and 516 , respectively (Fig. 4).

By monitoring the phase difference between the readout signal and the input signal, we can determine the shielding factor of the transfer function and the direction of the induce DC field. For low-frequency signals (e.g., 10 and 20 kHz), the transfer function shows a phase advance effect with a value of $\arctan(\gamma/\pi f)$, due to the low-frequency shielding effect. Based on the value of this advanced phase, we can calculate the amplitude of the transfer function (Methods). It should be noted that as the signal frequency increases (e.g., 60 and 100 kHz), limited by the atomic response speed, the phase lag phenomenon may gradually reduce the accuracy of this derivation method. Furthermore, we can also determine the direction of the induced DC field by observing the transmitted phase. When the initial electric field direction of the input signal is vertically downward (forward-fed), the phase of the readout signal is closer to that of the input signal, indicating that the direction of the induced DC electric field is also vertically downward. This allows us to indirectly infer that the charges accumulated on the cell wall are positive charges. Conversely, for reverse-fed signals, the phase of the output signal is inverted (Fig. 5).

Structural enhancement technology

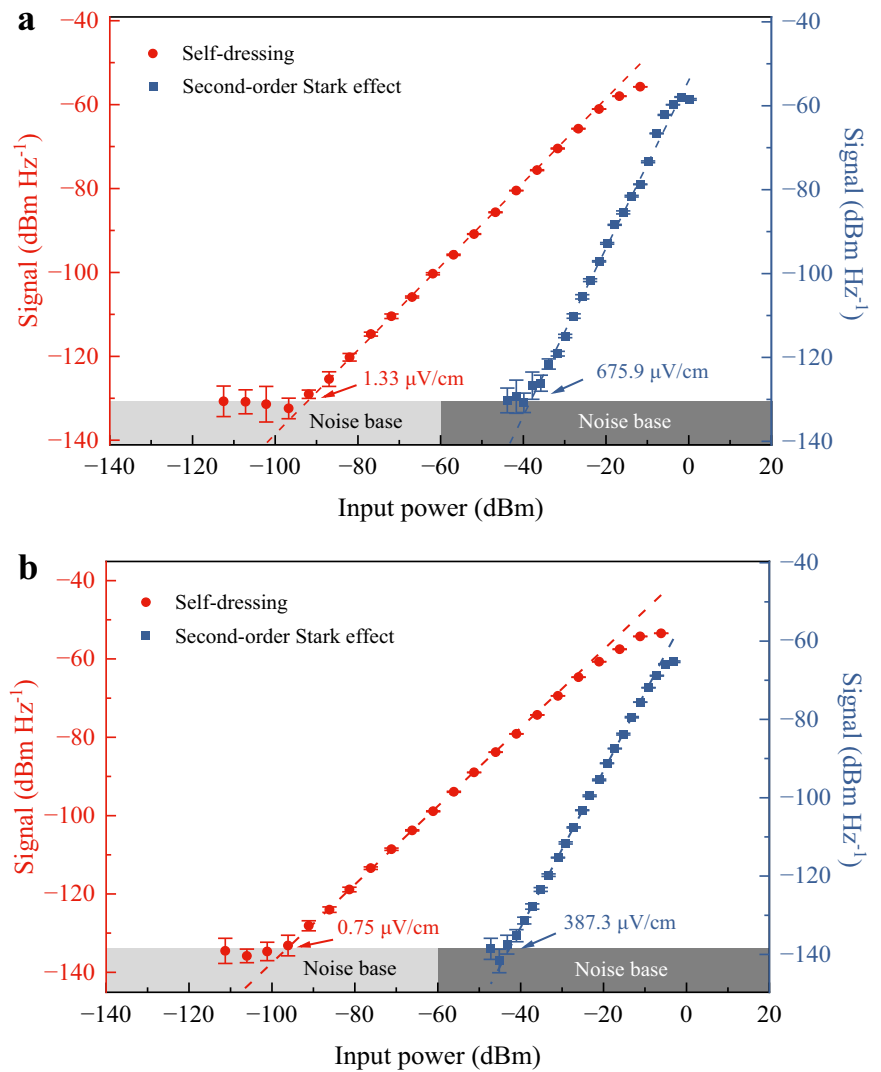
To further enhance the coupling capability of atomic sensors to spatial signals, this study designed a RES for kHz spatial signal manipulation. This structure is primarily used to capture the signal and regenerate the electric field after RES, generating a stronger signal electric field at the Rydberg atoms and thereby improving the sensitivity of the signal reception system (Methods).

Parallel plates with a terminating matched resistor were used to generate a spatial signal field, aiming to measure the sensitivity of the atomic sensor with the RES loaded. Since the detectable electric field strength is lower than the background noise level in space at this frequency band, here the measurement device was placed in a grounded shielding box with partial openings to allow laser beams and feeding wires to pass through (Methods). By adjusting the capacitance value on the structure, the operating frequency points of the RES can be tuned to 20 kHz and 100 kHz , respectively. At a spectrum analyzer resolution bandwidth of 1 Hz , the minimum detectable electric fields were 44.4 and $13.5 \text{ nV}/\text{cm}$, with corresponding sensitivities of 44.4 and $13.5 \text{ nV}/\text{cm}/\text{Hz}^{1/2}$ (Fig. 6). Compared with measurements without the structure loaded, the sensitivity of the atomic sensor at 20 and 100 kHz was improved by a factor of 30 and 56 , respectively.

Discussion

In summary, we proposed a Rydberg atom receiver architecture based on laser-induced DC field self-dressing. This architecture leverages sapphire to modify the adsorption dynamics of the inner cell walls, utilizing the DC field generated by coupling laser excitation to induce a self-dressing effect on atoms, thereby suppressing the impact of low-frequency shielding effects on the atomic receiver. By introducing structural enhancement technology, we further improved the receiver's coupling capability to spatial kHz signals, providing a critical technical pathway for achieving ultra-high-sensitivity

Fig. 4 | First-order detection based on the self-dressing effect and second-order detection. Sensitivity results measured at 20 kHz (a) and 100 kHz (b). Under the self-dressing effect, the signal amplitude input from the photodetector to the spectrum analyzer as a function of the power injected into the TEM cell by the signal source (red circles); red dashed lines represent the fitted trend of the first-order linear interval. The distance between the laser beam and the cell wall was adjusted to minimize the splitting of the $|52D_{5/2}\rangle$ energy level. At this point, the signal amplitude monitored at the second harmonic frequency as a function of the power injected into the TEM cell (blue squares) was used to evaluate the measurement capability of the second-order Stark effect; blue dashed lines represent the fitted trend of the second-order linear interval. Error bars in the figures represent the 1σ standard deviation from 5 measurements.



atomic receivers. By improving vapor cell fabrication processes to further reduce the adsorption of alkali metal atoms on the cell walls, the high-sensitivity measurement frequency range can be extended to lower frequencies. Combining techniques such as beam shaping, multi-atom systems, and high-angular-momentum quantum number excitation, it is expected to further enhance the sensitivity of atomic sensors while exhibiting the unique advantage of miniaturization.

Methods

Experimental setup

We employ a two-photon excitation scheme to excite cesium atoms to a Rydberg state. The probe laser, directly generated by a semiconductor laser with a wavelength of 852 nm, excites atoms from the ground state $|6S_{1/2}, F = 4\rangle$ to the excited state $|6P_{3/2}, F = 5\rangle$. The coupling laser of 509 nm excites atoms from the excited state $|6P_{3/2}, F = 5\rangle$ to the Rydberg state $|52D_{5/2}\rangle$. By scanning the frequency of the coupling laser, the EIT spectrum is obtained by monitoring the change in probe light power via a PD. The two laser beams are incident collinearly and oppositely into the vapor cell to mitigate the Doppler broadening of the EIT spectrum. Before entering the vapor cell, both beams pass through an HWP and a PBS, which allows for convenient adjustment of laser power and ensures that the lasers are vertically polarized at the position of the vapor cell (Fig. 1a). We lock the frequency of the probe laser using saturated absorption spectroscopy. Two sets of EIT spectra are excited simultaneously: one is used to lock the frequency of the coupling laser, and the other is used for experimental data testing.

Three-level atomic model

Considering the rotating-wave approximation and electric dipole approximation, the Hamiltonian of the three-level system in the interaction picture can be expressed as (in the basis of bare states $[|1\rangle, |2\rangle, |3\rangle]^T$):

$$H = \frac{\hbar}{2} \begin{pmatrix} 0 & \Omega_p & 0 \\ \Omega_p & -2\Delta_p & \Omega_c \\ 0 & \Omega_c & -2(\Delta_p + \Delta_c) \end{pmatrix} \quad (8)$$

When the frequencies of the probe laser and coupling laser are resonant with the corresponding energy levels, their eigenvalues are

$$E_{d1} = 0, E_{d2} = -\frac{\hbar}{2} \sqrt{\Omega_c^2 + \Omega_p^2}, E_{d3} = \frac{\hbar}{2} \sqrt{\Omega_c^2 + \Omega_p^2}$$

The corresponding three eigenstates are

$$\begin{aligned} |E_{d1}\rangle &= -\frac{\Omega_c}{\sqrt{\Omega_c^2 + \Omega_p^2}} |1\rangle + \frac{\Omega_p}{\sqrt{\Omega_c^2 + \Omega_p^2}} |3\rangle \\ |E_{d2}\rangle &= -\frac{\sqrt{2}\Omega_p}{2\sqrt{\Omega_c^2 + \Omega_p^2}} |1\rangle + \frac{\sqrt{2}}{2} |2\rangle + \frac{\sqrt{2}\Omega_c}{2\sqrt{\Omega_c^2 + \Omega_p^2}} |3\rangle \\ |E_{d3}\rangle &= \frac{\sqrt{2}\Omega_p}{2\sqrt{\Omega_c^2 + \Omega_p^2}} |1\rangle + \frac{\sqrt{2}}{2} |2\rangle - \frac{\sqrt{2}\Omega_c}{2\sqrt{\Omega_c^2 + \Omega_p^2}} |3\rangle \end{aligned} \quad (9)$$

Fig. 5 | Comparison of phases of time-domain signals. Time-domain signals measured at frequencies of 10 kHz (a), 20 kHz (b), 60 kHz (c), and 100 kHz (d). In the figures, solid lines represent the monitoring signals output by the signal source (MS). Solid scatter plots represent the time-domain signals output by the photodetector when the TEM cell is forward-fed (+fed). Hollow scatter plots represent the time-domain signals output by the photodetector when the TEM cell is reverse-fed (−fed) (Methods).

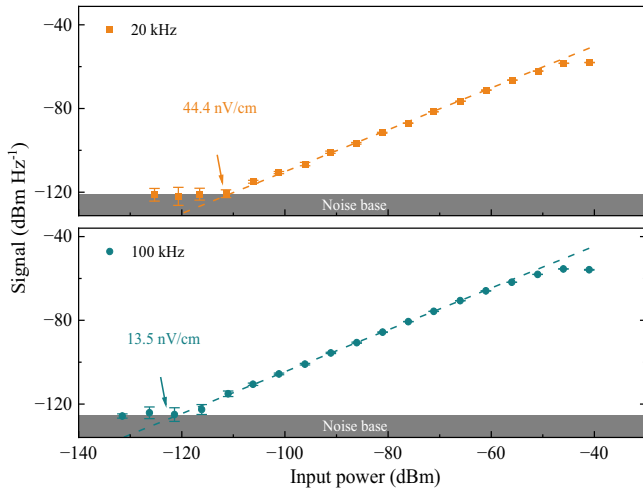
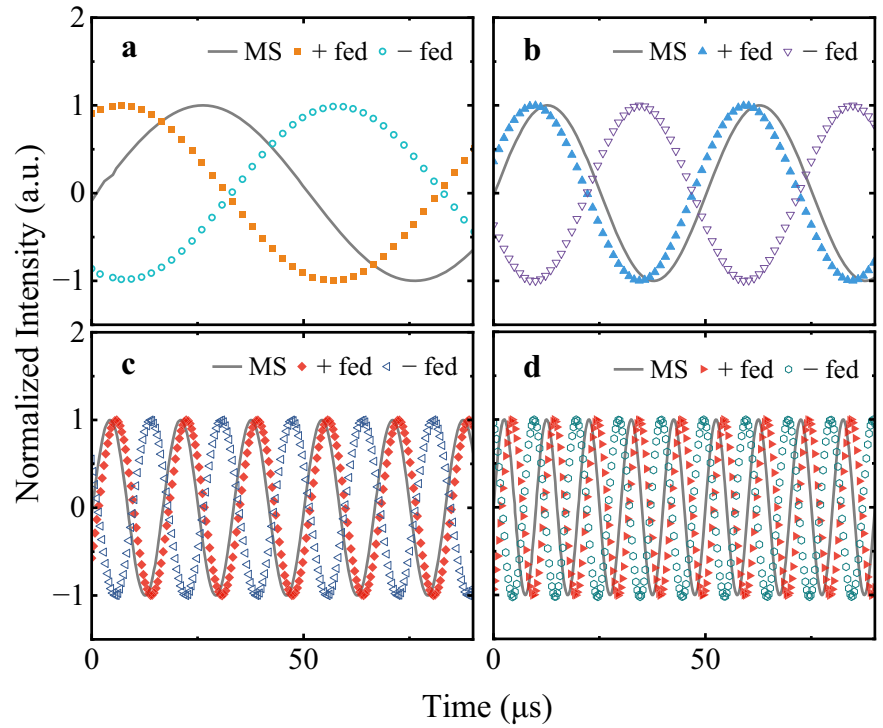


Fig. 6 | Sensitivity of the atomic receiver based on structural enhancement technology. The operating frequency of the resonant enhancement structure is adjusted using a tunable capacitor, and it is placed in a shielding box for sensitivity testing. During the test, the laser beam position and laser power are consistent with those set in Fig. 4. In the figure, the orange dashed line and green dashed line fit the variation trends of the first-order linear intervals at 20 kHz and 100 kHz, respectively.

Herein, $|E_{d1}\rangle$ consists only of the ground state $|1\rangle$ and Rydberg state $|3\rangle$, with a population probability of 0 in the excited state $|2\rangle$, thus being referred to as the dark state. In the dark state, the atomic vapor no longer absorbs the probe laser, thereby generating the EIT effect.

Considering the coupling between the quantum system and factors such as the environment, we use the Lindblad master equation method to analyze the losses caused by interaction with the environment, expressed as:

$$\dot{\rho} = -\frac{j}{\hbar}[H, \rho] + L(\rho) \quad (10)$$

where $L(\rho)$ is the Lindblad superoperator. The matrix representation is:

$$L(\rho) = \sum_m (L_m \rho L_m^\dagger - \frac{1}{2}(L_m^\dagger L_m \rho + \rho L_m^\dagger L_m)) \quad (11)$$

Here, L_m denotes the influence of a certain loss factor, and ρ is the density matrix, expressed as:

$$\rho = \begin{pmatrix} \rho_{11} & \rho_{12} & \rho_{13} \\ \rho_{21} & \rho_{22} & \rho_{23} \\ \rho_{31} & \rho_{32} & \rho_{33} \end{pmatrix} \quad (12)$$

Substituting Eqs. (11) and (12) above into Eq. (10), the corresponding optical Bloch equations of the system can be obtained. When the system reaches a steady state, the density matrix no longer changes, satisfying $\dot{\rho} = 0$. Combined with the requirement of $\rho_{11} + \rho_{22} + \rho_{33} = 1$ in the density matrix, the instantaneous steady-state solution of the Bloch equations can be derived.

Considering the thermal motion of the atoms themselves, the influence of the Doppler effect needs to be introduced into the analysis. In our experimental setup, the probe laser and coupling laser are incident oppositely, and their detuning can be corrected as:

$$\begin{aligned} \Delta'_p &= \Delta_p - \frac{2\pi v}{\lambda_p} \\ \Delta'_c &= \Delta_c + \frac{2\pi v}{\lambda_c} \end{aligned} \quad (13)$$

where v represents the motion velocity of atoms. The corrected result of the density matrix element ρ_{12} after Doppler averaging is given as:

$$\rho_{12D} = \frac{1}{\sqrt{\pi}v_p} \int_{-3v_p}^{3v_p} \rho_{12}(\Delta'_p, \Delta'_c) e^{-\frac{v^2}{v_p^2}} dv \quad (14)$$

where $v_p = \sqrt{2kT/m}$ is the most probable velocity of atoms, k is the Boltzmann constant, T is the operating temperature of the atomic vapor, and m is the atomic mass.

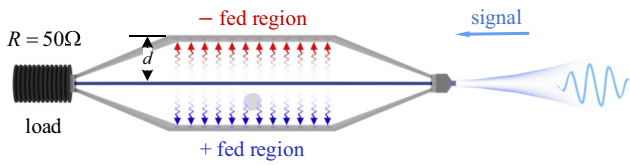


Fig. 7 | Standard electric field generation device of the TEM cell. The middle part of the device is a core plate, and the upper and lower parts are ground plates. The distance between the central part of the core plate and the ground plates is d for both. Based on the feeding characteristics, the internal space of the structure is divided into a $-$ fed region in the upper half and a $+$ fed region in the lower half.

According to the Beer–Lambert law, the probe laser transmitted through the atomic vapor cell can be expressed as:

$$P = P_0 \exp\left(-\frac{4\pi l N_0 \mu_p^2 \text{Im}[\rho_{21D}]}{\epsilon_0 \hbar \Omega_p \lambda_p}\right) \quad (15)$$

Since we obtain the probe laser transmission spectrum by scanning the frequency of the coupling laser, there is no need to correct for Doppler mismatch. However, the presence of the Doppler effects affect the broadening of the EIT spectrum and may reduce the slope β of the spectrum.

Control of DC field strength

As shown in Fig. 2a, the frequency shift of the sublevel exhibits an approximately linear relationship with the coupling laser power: $\Delta \Omega_j = -\alpha_j k P_c$, where the DC electric field E_{DC} satisfies $E_{DC} = \sqrt{2kP_c}$. Here, k denotes the field generation coefficient, whose value depends on factors such as the spatial relationship between the laser beam and the wall, the material of the cell shell, the geometric structure of the cell shell, and the density of alkali metal atoms.

When the coupling power is fixed, altering the spatial relationship between the laser beam and the cell wall constitutes the optimal approach to rapidly adjust the coefficient k . To ensure the DC electric field exerts the optimal enhancement effect on kHz signal reception, the laser beam is positioned slightly above the center of the cell, such that the direction of the DC electric field is collinear with the polarization directions of both the probe laser and the coupling laser. A lifting platform enables precise control over the distance between the cell wall and the laser beam, thereby regulating the DC electric field strength by influencing the coefficient k . Experimental results reveal significant differences in the DC electric fields corresponding to different cell materials. The k coefficient of the sapphire cell is significantly higher than that of the glass cell, allowing a stronger DC electric field to be generated in the sapphire cell under identical experimental conditions. Consequently, the self-dressing effect in kHz signal reception is achieved through the interaction between the coupling laser and the internal environment of the cell.

Derivation of the transfer function formula

The transfer function describes the variation of the external electric field after penetrating into the vapor cell in the frequency domain. Since the transfer function only characterizes changes in the amplitude and phase of the electric field, the amplitude and initial phase of the external electric field can be set to arbitrary values for analysis. Considering the external electric field as a unit step signal, the expression is given by:

$$E_{out}(t) = u(t) = \begin{cases} 0, & t < 0 \\ 1, & t \geq 0 \end{cases} \quad (16)$$

The frequency-domain expression, $E_{out}(f)$, is given by:

$$E_{out}(f) = F\{u(t)\} = 1/j2\pi f, \quad f > 0 \quad (17)$$

The frequency-domain expression of the internal signal $E_{in}(t)$ is denoted as $E_{in}(f)$, given by:

$$E_{in}(f) = F\{\exp(-t/1.5\epsilon R_{\square} r)\} = \frac{1}{1/(1.5\epsilon R_{\square} r) + j2\pi f} \quad (18)$$

By definition of the transfer function, $T(f)$ is given by:

$$T(f) = \frac{E_{in}(f)}{E_{out}(f)} = \frac{1/(1/(1.5\epsilon R_{\square} r) + j2\pi f)}{1/j2\pi f} = \frac{j2\pi f}{1/(1.5\epsilon R_{\square} r) + j2\pi f}, \quad f > 0 \quad (19)$$

When extended to vapor cells of general shapes, the frequency-domain expression of the internal electric field $E_{in}(f)$ is given by:

$$E_{in}(f) = F\{\exp(-2\gamma t)\} = \frac{1}{2\gamma + j2\pi f} \quad (20)$$

Thus, the expression for the transfer function $T(f)$ can be expressed as:

$$T(f) = \frac{E_{in}(f)}{E_{out}(f)} = \frac{1/(2\gamma + j2\pi f)}{1/j2\pi f} = \frac{j\pi f}{\gamma + j\pi f}, \quad f > 0 \quad (21)$$

The amplitude $|T(f)|$ of Eq. (21) is:

$$|T(f)| = \frac{|j\pi f|}{|\gamma + j\pi f|} = \frac{\pi f}{\sqrt{\gamma^2 + (\pi f)^2}} \quad (22)$$

The phase $\angle T(f)$ of Eq. (21) is given by:

$$\begin{aligned} \angle T(f) &= \angle(j\pi f) - \angle(\gamma + j\pi f) = \frac{\pi}{2} - \arctan(\pi f / \gamma) \\ &= \arctan(\gamma / \pi f) \end{aligned} \quad (23)$$

Thus, the transfer function $T(f)$ can also be expressed as:

$$T(f) = \frac{\pi f}{\sqrt{\gamma^2 + (\pi f)^2}} \cdot \exp(j\arctan(\gamma / \pi f)), \quad f > 0 \quad (24)$$

Electric field generation based on a TEM cell

As shown in Fig. 7, an open TEM cell with a characteristic resistance (R) of 50Ω was used to generate an electric field at kHz frequencies. The design of this TEM cell complies with the standard IEEE Std 1309™-2013. A voltage signal was injected into one end of the TEM cell via a coaxial cable. After passing through a tapered structure, an electric field with a calculable strength $E = \sqrt{PR}/d$ is formed in the middle of the TEM cell, where P denotes the injected power. After passing through the vapor cell, the electric field passed through another tapered structure and was absorbed by a 50Ω matching load at the end. The purpose of this operation was to make the electric field at the vapor cell position as uniform as possible and to more fully simulate the far-field propagation pattern of the kHz-frequency electric field.

Calculation of shielding factor and sheet resistance

After measuring the response curve of the Rydberg atom receiver to electric field signals with equal amplitude but different frequencies, the coefficient γ in the relation $|T(f)| = \pi f / \sqrt{\gamma^2 + (\pi f)^2}$ is treated as an undetermined parameter. The value of the shielding factor γ can be obtained by fitting the variation trends of the measured data and the theoretical curve using the orthogonal distance regression method. Another calculation approach involves first acquiring the phase difference $\Delta\phi$ between the signal received under forward feeding and the monitored signal, then calculating the

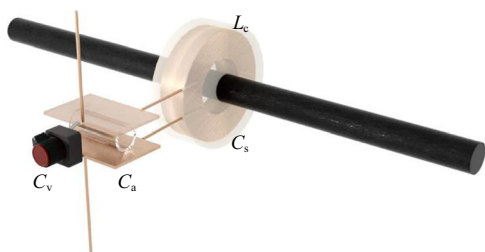


Fig. 8 | Resonant enhancement structure. The structure enables the coupling of spatial signals and forms LC resonance enhancement in the circuit. The vapor cell is located between the parallel metal plates, where the structure regenerates the enhanced electric field signal.

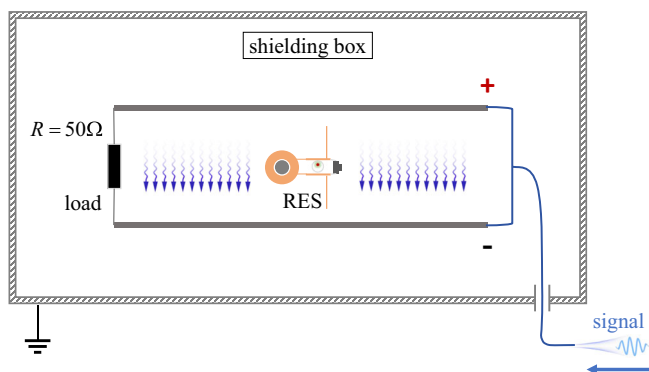


Fig. 9 | Sensitivity testing setup with electromagnetic noise shielding. The shielding box comprises a conductive outer casing, which is grounded to ensure superior shielding efficacy. Apertures at specific locations on the casing enable the passage of signal cables and laser beams. The electric field generation device employs a + fed configuration.

shielding factor using the formula $\gamma = \pi f \tan(\Delta\phi)$, and further deriving the value of $|T(f)|$.

When calculating the shielding factor γ of the glass vapor cell, it is difficult to determine γ by directly receiving kHz signals due to the significant influence of low-frequency shielding effects. Therefore, we adopt the spectral readout method to measure the second-order Stark shift induced by 1–20 MHz signals, determine the electric field strength inside the vapor cell, and further obtain the value of γ through fitting.

For the further calculation of sheet resistance, it is necessary to establish a sheet resistance film model consistent with the actual shape of the vapor cell. The response amplitude is calculated using a finite element algorithm, and optimization algorithms such as the trust region algorithm and genetic algorithm are employed to set the sheet resistance value in the model. This process continues until the response curve from numerical calculation is consistent with the measured data; the sheet resistance value set at this point is the result of the sheet resistance obtained via numerical calculation.

kHz resonant enhancement structure design

Given the extremely long wavelength of kHz signals, conventional half-wave RESs are impractical to implement. We therefore use a cored coil to form the inductive component L_c , and parallel metal plates—incorporating an external variable capacitor C_v and a capacitive electric field coupling structure—to form the capacitive component (Fig. 8). This configuration creates a resonant circuit with reactance cancellation, where the parallel metal plates regenerate the resonance-enhanced signal into a spatial electric field for reception by Rydberg atoms. The total capacitance in the circuit is $C_{\text{all}} = C_a + C_v + C_s$, where C_a is the capacitance introduced by the electric field coupling structure and parallel metal plates, and C_s is the stray capacitance introduced by the coil. The resonance condition is

$f_0 = 1/2\pi\sqrt{L_c C_{\text{all}}}$, where f_0 denotes the optimal operating frequency. The f_0 of the structure can be adjusted by tuning the C_v .

The coil in this work is wound using a honeycomb winding method to minimize losses from stray capacitance. This coil has an inner diameter of 20 mm, a height of 10 mm, and 1010 turns. The magnetic core used is cylindrical, with a length of 200 mm, a diameter of 10 mm, and a relative permeability of 2200. The capacitive electric field coupling structure has a diameter of 1 mm and a single-arm length of 35 mm.

Measurement of atomic receiver sensitivity based on structural enhancement

Following the integration of the external structure, the Rydberg atomic receiver exhibits a pronounced detectable electric field intensity even below the ambient electromagnetic noise in the spatial environment. Therefore, the sensitivity measurement is realized inside a shielding box to prevent interference from external noise signals. A parallel metal plate electrode is constructed as the signal electric field generation device (Fig. 9). Analogous to the TEM cell described earlier, a 50 Ω matching resistor is terminated at the end of the signal transmission path to absorb excess signal energy, with the electric field strength expressed as $E = \sqrt{PR/d}$.

Data availability

The data supporting the findings of this study are available within this article. Additional data are available from the corresponding author on reasonable request.

Received: 2 September 2025; Accepted: 26 January 2026;

Published online: 10 February 2026

References

- Jing, M. Y. et al. Atomic superheterodyne receiver based on microwave-dressed Rydberg spectroscopy. *Nat. Phys.* **16**, 911–915 (2020).
- Wu, S. H. et al. Quantum magnetic gradiometer with entangled twin light beams. *Sci. Adv.* **9**, eadg1760 (2023).
- Chen, X. D. et al. Quantum enhanced radio detection and ranging with solid spins. *Nat. Commun.* **14**, 1288 (2023).
- Carmiggelt, J. J. et al. Broadband microwave detection using electron spins in a hybrid diamond-magnet sensor chip. *Nat. Commun.* **14**, 490 (2023).
- Wang, P. F. et al. High-resolution vector microwave magnetometry based on solid-state spins in diamond. *Nat. Commun.* **6**, 6631 (2015).
- Pieplow, G. et al. Quantum electrometer for time-resolved material science at the atomic lattice scale. *Nat. Commun.* **16**, 6435 (2025).
- Bonus, F. et al. Ultrasensitive single-ion electrometry in a magnetic field gradient. *Nat. Phys.* **21**, 1189–1195 (2025).
- Gonzalez-Zalba, M. F., Barraud, S., Ferguson, A. J. & Betz, A. C. Probing the limits of gate-based charge sensing. *Nat. Commun.* **6**, 6084 (2015).
- Stray, B. et al. Quantum sensing for gravity cartography. *Nature* **602**, 590–594 (2022).
- Shettell, N. et al. Geophysical survey based on hybrid gravimetry using relative measurements and an atomic gravimeter as an absolute reference. *Sci. Rep.* **14**, 6511 (2024).
- Panda, C. D. et al. Measuring gravitational attraction with a lattice atom interferometer. *Nature* **631**, 515–520 (2024).
- Meyer, D. H., Castillo, Z. A., Cox, K. C. & Kunz, P. D. Assessment of Rydberg atoms for wideband electric field sensing. *J. Phys. B. Mol. Opt. Phys.* **53**, 1–12 (2020).
- Anderson, D. A., Sapiro, R. E. & Raithel, G. A self-calibrating SI-traceable broadband Rydberg atom-based radio-frequency electric field probe and measurement instrument. *IEEE Trans. Antennas Propag.* **69**, 5931–5941 (2021).
- Holloway, C. L. et al. Broadband Rydberg atom-based electric-field probe for SI-traceable, self-calibrated measurements. *IEEE Trans. Antennas Propag.* **62**, 6169–6182 (2014).

15. Anderson, D. A. et al. Optical measurements of strong microwave fields with Rydberg atoms in a vapor cell. *Phys. Rev. Appl.* **5**, 034003 (2016).
16. Li, Y. X. et al. A compact tunable enhancement resonator for Rydberg atomic receiver. *IEEE Antennas Wirel. Propag. Lett.* **24**, 808–812 (2025).
17. Robinson, A. K., Prajapati, N., Senic, D., Simons, M. T. & Holloway, C. L. Determining the angle-of-arrival of a radio-frequency source with a Rydberg atom-based sensor. *Appl. Phys. Lett.* **118**, 1–5 (2021).
18. Ding, Z. K. et al. A circularly-polarized omnidirectional Rydberg atomic sensor using characteristic mode analysis. *IEEE Trans. Antennas Propag.* **72**, 1 (2024).
19. Cai, Y. F. et al. High-sensitivity Rydberg-atom-based phase-modulation receiver for frequency-division-multiplexing communication. *Phys. Rev. Appl.* **19**, 044079 (2023).
20. Mao, R. Q., Lin, Y., Fu, Y. Q., Ma, Y. M. & Yang, K. Digital beamforming and receiving array research based on Rydberg field probes. *IEEE Trans. Antennas Propag.* **72**, 2025–2029 (2024).
21. Yang, K. et al. Local oscillator port-integrated resonators for sensitivity enhancement of VHF band Rydberg atomic heterodyne receivers. *IEEE Trans. Microw. Theory Tech.* **73**, 1–10 (2025).
22. Tu, H. T. et al. Approaching the standard quantum limit of a Rydberg-atom microwave electrometer. *Sci. Adv.* **10**, eads0683 (2024).
23. Cai, M. H., You, S. H., Zhang, S. S., Xu, Z. S. & Liu, H. P. Sensitivity extension of atom-based amplitude-modulation microwave electrometry via high Rydberg states. *Appl. Phys. Lett.* **122**, 161103 (2023).
24. Cai, M. H., Xu, Z. S., You, S. H. & Liu, H. P. Sensitivity improvement and determination of Rydberg atom-based microwave sensor. *Photonics* **9**, 250 (2022).
25. Koziel, S., Pietrenko-Dabrowska, A. & Ullah, U. Global miniaturization of broadband antennas by prescreening and machine learning. *Sci. Rep.* **14**, 29427 (2024).
26. Maksimenko, A. et al. Miniaturization limits of ceramic UHF RFID tags. *Sci. Rep.* **15**, 10984 (2025).
27. Nan, T. X. et al. Acoustically actuated ultra-compact NEMS magnetoelectric antennas. *Nat. Commun.* **8**, 296 (2017).
28. Cox, K. C., Meyer, D. H., Fatemi, F. K. & Kunz, P. D. Quantum-limited atomic receiver in the electrically small regime. *Phys. Rev. Lett.* **121**, 110502 (2018).
29. Mao, R. Q., Lin, Y., Zhou, A. J., Yang, K. & Fu, Y. Q. Shortwave ultra-high sensitivity Rydberg atomic electric field sensing based on a subminiature resonator. *IEEE Trans. Antennas Propag.* **72**, 1 (2024).
30. Rotunno, A. P. et al. Detection of 3–300 MHz electric fields using Floquet sideband gaps by “Rabi matching” dressed Rydberg atoms. *J. Appl. Phys.* **134**, 134501 (2023).
31. Lei, M. W. & Shi, M. High-sensitivity measurement of ULF, VLF, and LF fields with a Rydberg-atom sensor. *Opt. Lett.* **49**, 5547–5550 (2024).
32. Li, L. et al. Super low-frequency electric field measurement based on Rydberg atoms. *Opt. Express* **31**, 29228–29234 (2023).
33. Jau, Y. Y. & Carter, T. Vapor-cell-based atomic electrometry for detection frequencies below 1 kHz. *Phys. Rev. Appl.* **13**, 054034 (2020).
34. Bouchiat, M. A., Guena, J., Jacquier, P., Lintz, M. & Papoyan, A. V. Electrical conductivity of glass and sapphire cells exposed to dry cesium vapor. *Appl. Phys. B-Lasers O.* **68**, 1109–1116 (1999).
35. Carter, J. D. & Martin, J. D. D. Energy shifts of Rydberg atoms due to patch fields near metal surfaces. *Phys. Rev. A* **83**, 032902 (2011).
36. Ma, L., Paradis, E. & Raithele, G. DC electric fields in electrode-free glass vapor cell by photoillumination. *Opt. Express* **28**, 3676–3685 (2020).
37. Sedlacek, J. A. et al. Electric field cancellation on quartz by Rb adsorbate-induced negative electron affinity. *Phys. Rev. Lett.* **116**, 133201 (2016).
38. IEEE. IEEE standard for calibration of electromagnetic field sensors and probes (excluding antennas) from 9 kHz to 40 GHz. *IEEE Std. 1309™-2013* (2013).

Acknowledgements

This study was funded by the National Natural Science Foundation of China (Grant No. U24B2009).

Author contributions

J.Z. and Z.S. contributed equally to this work and are considered co-first authors. Y.F. and Q.A. conceived the idea of self-enhanced Rydberg atomic heterodyne electrometry via laser induced dc dressing. J.Z., Z.S., and J.Y. laid the theoretical foundation for this concept. Y.L., D.S., and K.Y. designed and fabricated the resonant enhancement structure. J.Z. and Z.S. designed the experimental setup and methods. J.Z., J.Y., and F.Z. constructed the experimental apparatus, conducted the experiments, and performed data analysis. All authors have contributed to the interpretation of the data and the drafting as well as the revision of the manuscript.

Competing interests

The authors declare no competing interests.

Additional information

Correspondence and requests for materials should be addressed to Qiang An or Yunqi Fu.

Reprints and permissions information is available at <http://www.nature.com/reprints>

Publisher's note Springer Nature remains neutral with regard to jurisdictional claims in published maps and institutional affiliations.

Open Access This article is licensed under a Creative Commons Attribution-NonCommercial-NoDerivatives 4.0 International License, which permits any non-commercial use, sharing, distribution and reproduction in any medium or format, as long as you give appropriate credit to the original author(s) and the source, provide a link to the Creative Commons licence, and indicate if you modified the licensed material. You do not have permission under this licence to share adapted material derived from this article or parts of it. The images or other third party material in this article are included in the article's Creative Commons licence, unless indicated otherwise in a credit line to the material. If material is not included in the article's Creative Commons licence and your intended use is not permitted by statutory regulation or exceeds the permitted use, you will need to obtain permission directly from the copyright holder. To view a copy of this licence, visit <http://creativecommons.org/licenses/by-nc-nd/4.0/>.

© The Author(s) 2026